Geometrical comparison of photonic crystal fiber-based surface plasmon resonance sensors

Ahmet Yasli
Huseyin Ademgil

Geometrical comparison of photonic crystal fiber-based surface plasmon resonance sensors

Ahmet Yasli and Huseyin Ademgil*
European University of Lefke, Faculty of Engineering, Department of Computer Engineering, Lefke, Northern Cyprus, Mersin, Turkey

Abstract. Numerical analysis and comparison of surface plasmon resonance (SPR)-based photonic crystal fiber (PCF) structures are presented. Full vectorial finite-element method (FEM) is employed to model and compare circular, elliptical, and square air hole-based PCF structures. The key propagation features, such as phase matching, sensitivity, resolution, and confinement loss behaviors of proposed structures, are reported. The effects of geometrical and design parameters are discussed and compared thoroughly. It is found that the sensitivity of circular air hole-based structure can reach up to 4200 nm/RIU, and the sensor resolution is 2.4×10^{-5} RIU. © 2018 Society of Photo-Optical Instrumentation Engineers (SPIE) [DOI: 10.1117/1.OE.57.3.030801]

1 Introduction

Surface plasmon resonance is a robust and effective technique of direct sensing. This unique technique was found to be one of the most effective methods of detecting the surface and interface effects. The SPR phenomenon can be described in terms of a collective oscillation in the free electron plasma at a metal boundary. These oscillations are caused by an electric field.[1,2] In the case of metal/liquid interface, the plasmons offer attractive applications in biosensing and chemical sensing. In recent years, SPR-based sensing has become a vital method for biochemical analysis without the use of labeled molecules in frontiers such as environmental protection, medical diagnostics, food care, and medication.[3] First, Jorgenson et al.[1] have introduced the optical fiber-based SPR sensor for chemical sensing applications. Accompanied by the photonic crystal fiber (PCF) (microstructured optical fiber) technology,[4] a new era has clearly begun for optical sensing.

Initially, the optical sensor structure proposed by Hassani et al.[5] has combined the PCF technology with the SPR technique. Due to its compact size, geometrical flexibilities, high degree of integration, high sensitivity, low propagation loss, and real-time detection ability, PCF-based SPR sensors are desirable for many sensor types, such as bio,[6] chemical,[7] temperature,[8] and refractive index sensors.[3]

SPR sensors are constructed by the principle of Kretschmann Raether prism geometry.[9] According to this geometry, by applying the conventional total internal reflection (TIR) rule, the incident light that goes into the prism will reflect back from the sides of the metallic layer while some amount of this incident light would be absorbed by plasmons (electron charge oscillations) from the metallic layer and couple between photons, which generates surface plasmon waves (SPW). On the evanescent field, when core and plasmonic mode refractive indices become mathematically equal to each other, resonance phase matching will occur, where

the maximum energy transfer from core mode to SPWs occurs. A sharp loss peaks are indicating the phase matching wavelength that allows the detection of sample analyte. If the refractive index of the analyte changes, the effective refractive index of SPW will also change and due to this change the peak point of loss will shift to a different wavelength. In this regard, the shift on peak point of the loss is the main source of the spectral interrogation method to sense differences on the analyte refractive indices.[10,11]

On the other hand, Kretschmann Raether prism geometry sensors have limited remote sensing capabilities and, due to their mechanical and optical requirements, they are bulky. These limitations can be overcome by exploring optical fiber-based SPR sensors. The unique propagation features, design flexibility, small size, and ability to control evanescent field brands PCFs are ideal candidates for sensing applications.[12] In addition, the performance of the PCF-based sensors are possible by optimizing the structural parameters, such as hole-to-hole spacing, cladding geometry, and hole diameter.[12–14]

The PCF structures are under study since the late 1990s. In this regard, various PCF structures with different air hole arrangements (square,[15] octagonal,[16] and decagonal[17]) have been studied and compared thoroughly. Further studies on PCF structures have shown that interesting propagation features can also be achieved with square-[18] and elliptical-[12] shaped cladding holes. First, Ref. 5 proposed PCF-based SPR sensor with circular air holes arranged in hexagonally, covered with gold metallic layers inside the silica. In contrast, Zhang et al.[19] have proposed a PCF-based SPR pressure sensor with all elliptical shape, silver-coated air holes in the cladding region. Furthermore, Wang et al.[20] have theoretically compared the effects of the various shaped (elliptical, square, and circular) silver nanowires for octagonal PCF-based SPR temperature sensor. It is found that the elliptical-based model shows a more obvious peak shift and higher sensitivity compared with other geometries.[20] Previous research have shown that the PCF-based SPR sensor

*Address all correspondence to: Huseyin Ademgil, E-mail: hademgil@eul.edu.tr

sensitivity and range can be enhanced by changing the structural (geometrical) parameters of design such as quantity, size, location, and shape of the air holes. Moreover, analyte channel size, thickness of metallic layer, and type of metal used are directly affecting the sensor performance.[13,14,21] The sensing performance depends highly on the choice of plasmonic materials where in most cases, gold and silver are used. Gold as a plasmonic material is more stable in an aqueous environment, whereas the resonance peak is wider, which may reduce sensing performance. Alternatively, silver has a sharper resonance peak but is more sensitive to an aqueous environment in terms of oxidation. For this reason, a graphene layer can be used between the analyte and silver layer to protect silver layer from oxidation.[14] However, on fabrication point of view this technique is more challenging compared with a single gold layer.

In brief, the propagation of core-guided leaky modes strongly depend on the pattern (square, hexagonal, or octagonal) and the geometrical shape of the cladding holes (circular, square, and elliptical). In contrast, interaction properties at resonance condition depend on the metallic layer (gold, silver, or graphene).[7,14,21–23] Taking all these into account, in this work, the effects of the various geometrical-shaped air holes (elliptical, circular, and square) on the performance of the proposed PCF-based SPR sensor against various analytes (1.33, 1.34, and 1.35) are investigated and compared
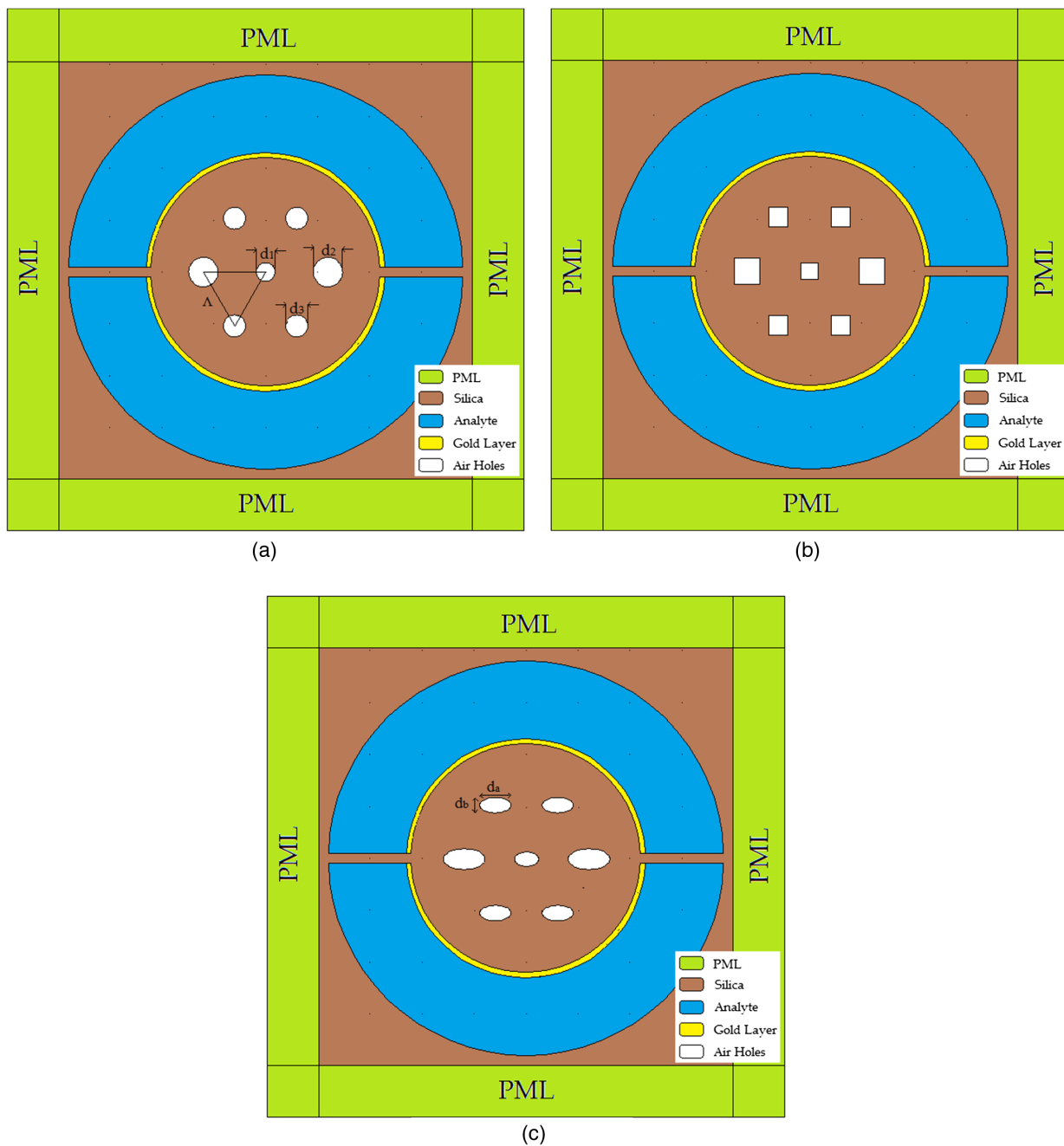

Fig. 1 Schematic diagrams of designed PCF-based SPR sensors: (a) circular-shaped air holes, (b) square-shaped air holes, and (c) elliptical-shaped air holes.

with previous studies. Figure 1 shows the proposed SPR sensor structures with hexagonal pattern. The proposed structure contains a central air hole to facilitate phase matching between guided and plasmon modes, two metalized microfluidic slots, and six various sized air holes for guiding the light.

A brief theory regarding PCF SPR biosensors is given in Sec. 2, which will be followed by the discussion of simulation results and, finally, conclusions in Sec. 4.

2 Numerical Modeling

In this study, the very well-known full vectorial finite-element method (FV-FEM) is employed for numerical modeling of the proposed SPR sensor.[11,12,21,24–26] The propagation behavior of the leaky modes is investigated by employing the anisotropic perfectly matched layers (PMLs) as boundary conditions, whereas whole PCF structure is divided into triangular subdomains (mesh elements). The numerical modeling carried out with COMSOL Multiphysics software, where a total of 12288 mesh elements are used for FEM analysis.

According to TIR, when the angle of incident of the incoming light is greater than the critical angle, the light is reflecting back from the gold layer toward the PCF core. However, practically a very small amount of light is refracting from the metallic layer, which generates the evanescent field and those refracted photons couple with electron charge oscillations (plasmon) at the surface of metal layer, which are known as SPWs. On the evanescent field when the resonance phase matching occurs between plasmon and core modes, SPW excites.[25] The confinement loss is expected to reach the highest level at the phase matching period. These sharp rises in the confinement loss are used by wavelength or spectral interrogation methods as a main source to detect changes on analyte. The following equation is used to calculate the confinement losses:[12,14,21,24]

$$\frac{40\pi}{\ln(10)\lambda}\operatorname{Im}(n_{\text{eff}}) \times 10^4 [\text{dB/cm}], \tag{1}$$

where $\operatorname{Im}(n_{\text{eff}})$ is the imaginary part of effective refractive index is and λ is the operating wavelength.

The sensitivity of SPR sensors is depending on their loss characteristics. So, the peak shifts are used to detect differences on analyte to find the sensitivity S with respect to wavelength or spectral interrogation method as calculated by the equation given as[26]

$$S(\lambda) = \frac{\Delta\lambda_{\text{peak}}}{\Delta n_a} (\text{nm/RIU}), \tag{2}$$

where $\Delta\lambda_{\text{peak}}$ are the differences on the position of resonance peaks, and Δn_a are the refractive indices of analytes.

The calculation of refractive index resolution (R) for proposed SPR sensors is carried out with the following equation:[27]

$$R = \Delta n_a \frac{\Delta\lambda_{\text{min}}}{\Delta\lambda_{\text{peak}}}, \tag{3}$$

where the resolution of instrumental peak wavelength is $\Delta\lambda_{\text{min}}$.

As can be seen from Fig. 1, proposed PCF-based SPR sensors contain seven altered sized air holes arranged hexagonally on silica background, which is surrounded by gold (Au) layers and analyte channel layers. The air holes sizes are denoted as d_1, d_2, and d_3 and these values are varying for each structure. The hole-to-hole spacing Λ is set to 1.2 μm for all structures. To make a strong comparison, the number of air holes and the position of the air holes are kept fixed for all structures. The refractive index values of analytes (n_a) are 1.33, 1.34, and 1.35. The permittivity of the gold is taken from Johnson and Christy Data,[28] with initially 40-nm gold layer thickness (t_{AU}). Also, the Sellmeier equation is used to model the silica that used for background material.[21]

Initially, as can be seen from Fig. 1(a), the SPR sensor with circular air holes in the cladding region is designed. To break the symmetry of the structure and achieve birefringence, the side holes are slightly larger than the other cladding holes. This way, the refractive index values of x- and y-polarized modes will be dissimilar. This phenomenon can be beneficial for multianalyte/multichannel sensing.[29] In this respect, the diameters of circular air holes are set as $d_1 = 0.359$ μm, $d_2 = 0.565$ μm, and $d_3 = 0.424$ μm, whereas the air hole areas are $\sim$0.10 $(\mu\text{m})^2$, 0.25 $(\mu\text{m})^2$, and 0.14 $(\mu\text{m})^2$, respectively. Based on a circular air holed model, elliptical- and square-holed models are designed with similar design parameters. To make reasonable comparison, the air hole areas are equalized for all models. For the elliptical structure, the ellipticity constant η is defined as the ratio of d_b/d_a and is fixed to 0.5. In this work, only the x- and y-polarized fundamental modes (HE_{11}^x and HE_{11}^y) are considered.

3 Numerical Results and Discussion

Figure 2 shows the distribution of an effective refractive index of the x-polarized fundamental core mode and the plasmon mode of the elliptical air-holed PCF-SPR sensor model, where $n_a = 1.33$ analyte. It can be evidently seen from the figure that fundamental core mode (blue dashed dotted line)
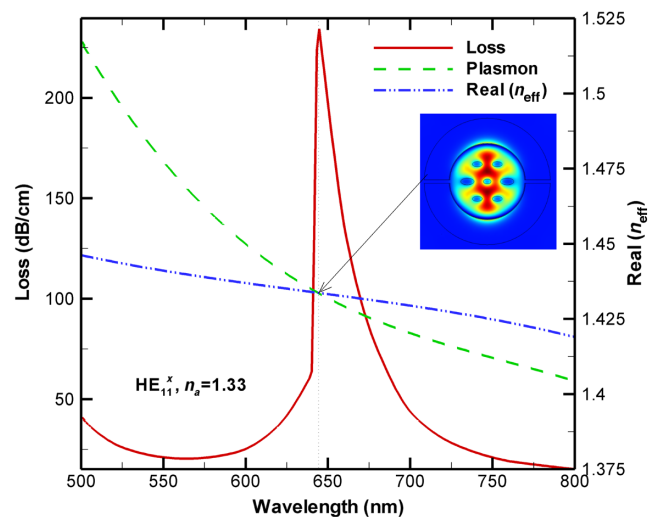
Fig. 2 Distribution of effective indices of plasmon and real part of fundamental modes versus loss for elliptical-based PCF-SPR sensor at the phase matching point for HE_{11}^x [$n_a = 1.33$, $t_{\text{AU}} = 40$ nm, $d_{1\text{area}} = 0.10$ $(\mu\text{m})^2$, $d_{2\text{area}} = 0.25$ $(\mu\text{m})^2$, and $d_{3\text{area}} = 0.14$ $(\mu\text{m})^2$].
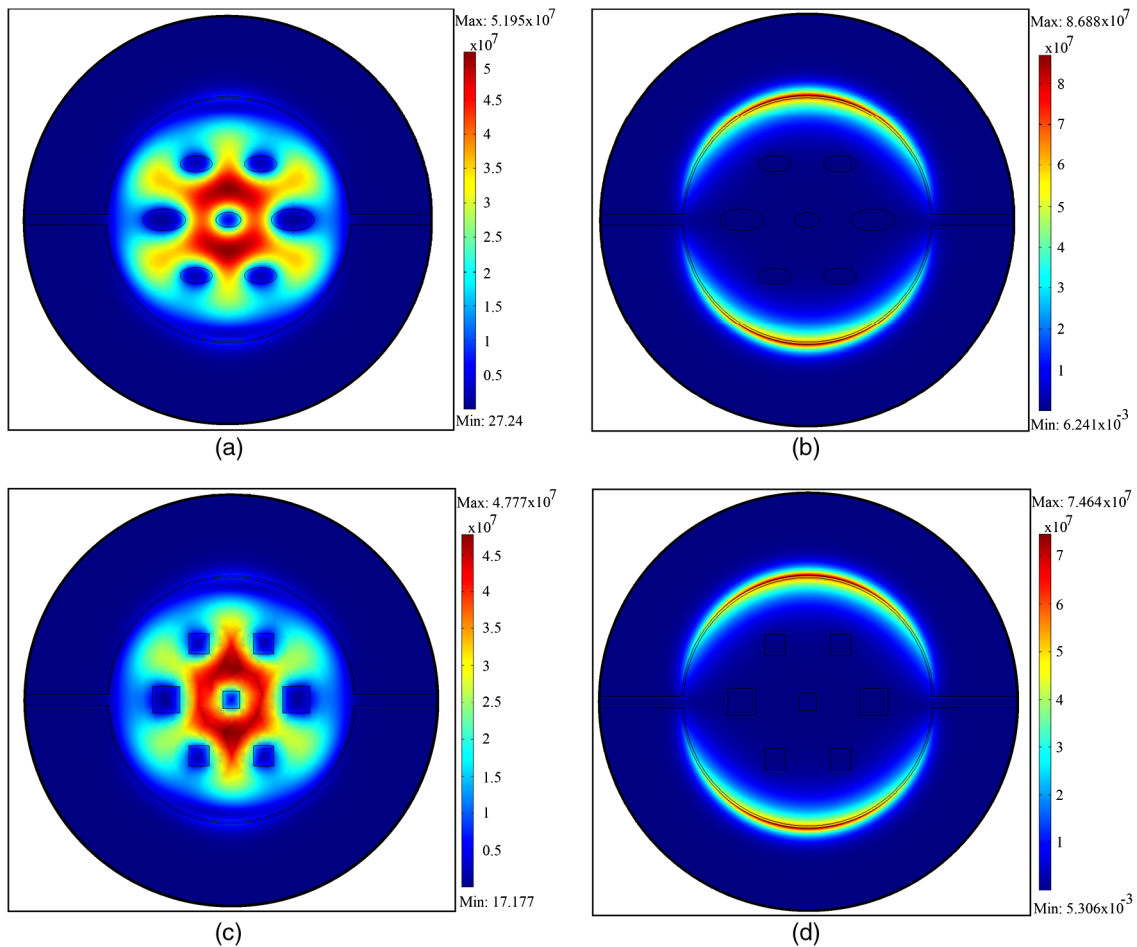
Fig. 3 Magnetic field distribution of: (a) elliptical hole-based model fundamental mode for HE^x_{11}. ($n_{eff} = 1.442076 - 2.217002e - 4i$), (b) elliptical hole-based model x-polarized plasmon mode ($n_{eff} = 1.486607 - 0.033094i$), (c) square hole-based model fundamental mode for HE^x_{11}. ($n_{eff} = 1.442977 - 2.142901e - 4i$), and (d) square hole-based model x-polarized plasmon mode ($n_{eff} = 1.486608 - 0.033097i$), where [surface: magnetic field norm (A/m), $\lambda = 540$ nm, $n_a = 1.33$, $t_{AU} = 40$ nm, $d_{1area} = 0.10$ (μm)^2, $d_{2area} = 0.25$ (μm)^2, and $d_{3area} = 0.14$ (μm)^2].

and the plasmon mode (green dashed line) are intersecting at $\lambda = 644$ nm. As described earlier in Sec. 2, resonance phase matching is occurred at this wavelength. Therefore, as can be seen from the figure, the confinement loss (red solid line) of the proposed model reaches the peak value at this specific operating wavelength.

The magnetic field distribution for core-guided x-polarized fundamental mode and plasmon mode is shown in Figs. 3(a) and 3(b), respectively, when $n_a = 1.33$ at $\lambda = 540$ nm. It can be observed from these figures that the magnetic field of core mode is concentrated at the core region, where relatively much light leakage occurs toward the channels. The plasmon mode also concentrates on the sides of gold layers, and there is no influence between core regions for that wavelength. At longer wavelengths ($\lambda = 644$ nm), leaked light will interact with free electrons on evanescent field, where resonance phase matching occurs. The magnetic field distributions for square air-holed structure are also presented in Figs. 3(c)–3(d). It can be seen that light shows similar behavior as elliptical-based model. In contrast, due to cornered nature of the square air holes the field pattern contains sharper edges when the light mode reflects from these square-shaped cladding holes. Also, the effective index of

the fundamental mode is slightly lower than the elliptical-based model.

Figures 4(a)–4(c) show the loss characteristics of fundamental modes (HE^x_{11} and HE^y_{11}) of proposed (a) circular, (b) square, and (c) elliptical air hole-based PCF-SPR sensors. The performances are evaluated when the analyte channels are filled with a refractive index of $n_a = 1.33$, $n_a = 1.34$, and $n_a = 1.35$. It can be seen from the figure that x-polarized mode has lower losses than y-polarized mode for all cases except square air hole-based model, where leakage on x-polarized mode is slightly higher for 1.33 analyte. It can also be seen that loss levels are varying with the air hole geometry, where square-based sensor exhibits lower losses. The change in analyte and air hole geometry leads the loss peak at resonance to shift, where peaks are associated with the phase matching points between the core modes and plasmon modes. It can also be seen that maximum difference between peak points is realized on circular and square air hole-based models for y- and x-polarizations, respectively, where this is an indication of higher sensitivity rate. The summary of these results can be seen in Fig. 4(d), where the loss peaks (resonant wavelengths) for studied analytes have linear distribution for all types of geometries.
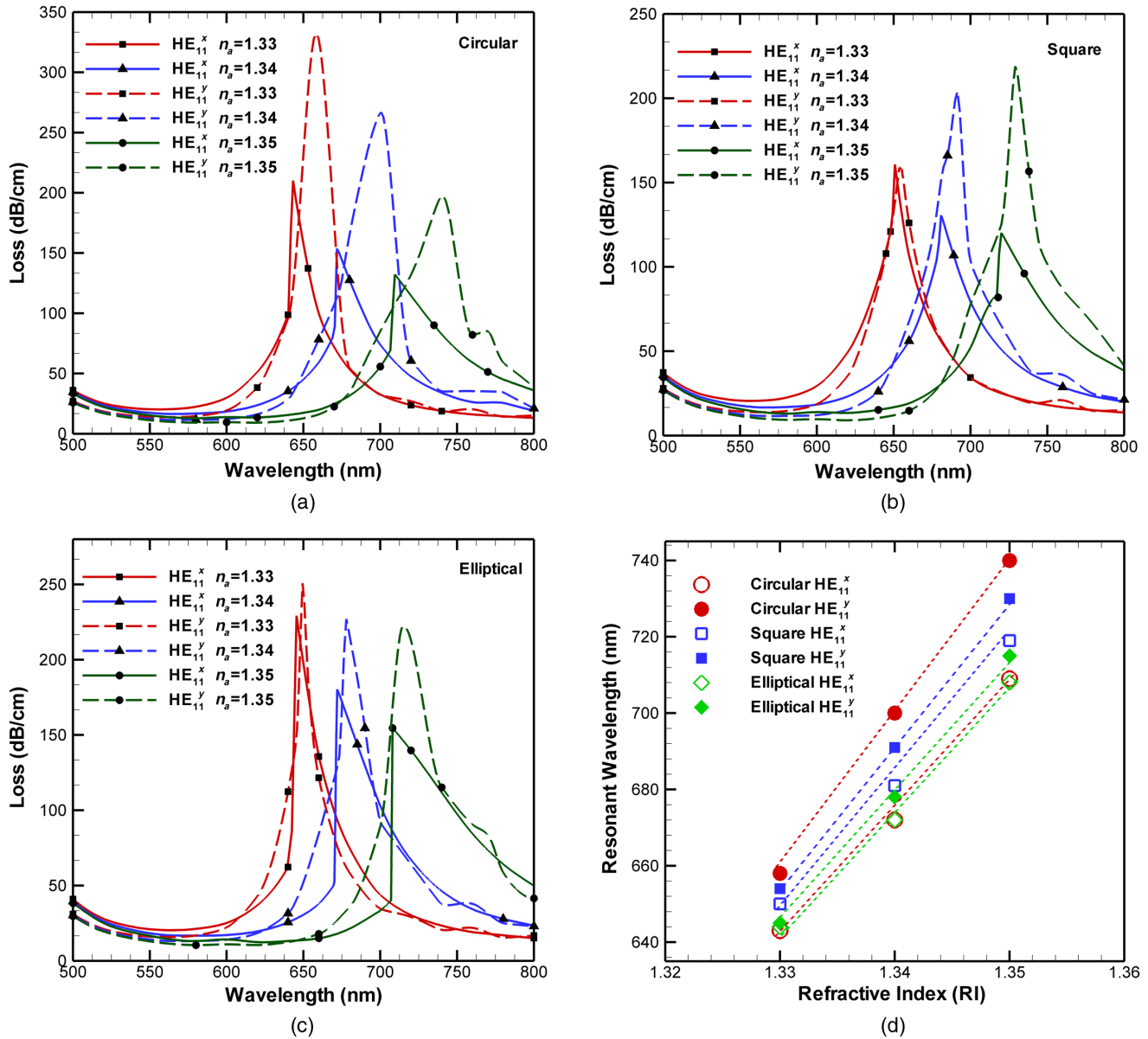
Fig. 4 Loss characteristics of fundamental core *x*-polarized HE$_{11}$ and *y*-polarized HE$_{11}$: (a) circular, (b) square, and (c) elliptical air hole-based PCF-SPR sensor designs, (d) the effect of refractive index change to resonance wavelength. [t_{AU} = 40 nm, d_{1area} = 0.10 (μm)^2, d_{2area} = 0.25 (μm)^2, d_{3area} = 0.14 (μm)^2].

The PCF-SPR sensor sensitivity is based on sensing the differences in analyte refractive index values. To find these differences, the sensitivity analysis of proposed sensors has been completed according to the spectral interrogation method. Considering the results presented in Fig. 4, a brief comparison of the proposed models is shown in Table 1.

Table 1 confirms that square and circular air hole-based models show better performance in terms of sensitivity. Moreover, owing to its asymmetric structure, *y*-polarized modes are much sensitive than *x*-polarized modes for all structures.

Gold is chemically stable in various environments such as aqueous water and shows the higher resonance shift.[30] The gold layer thickness is one of the most critical geometrical parameters to adjust the interaction of the analyte with polarization of light. Although SPW propagating along

Table 1 Sensitivity and resolution results for PCF-SPR model.

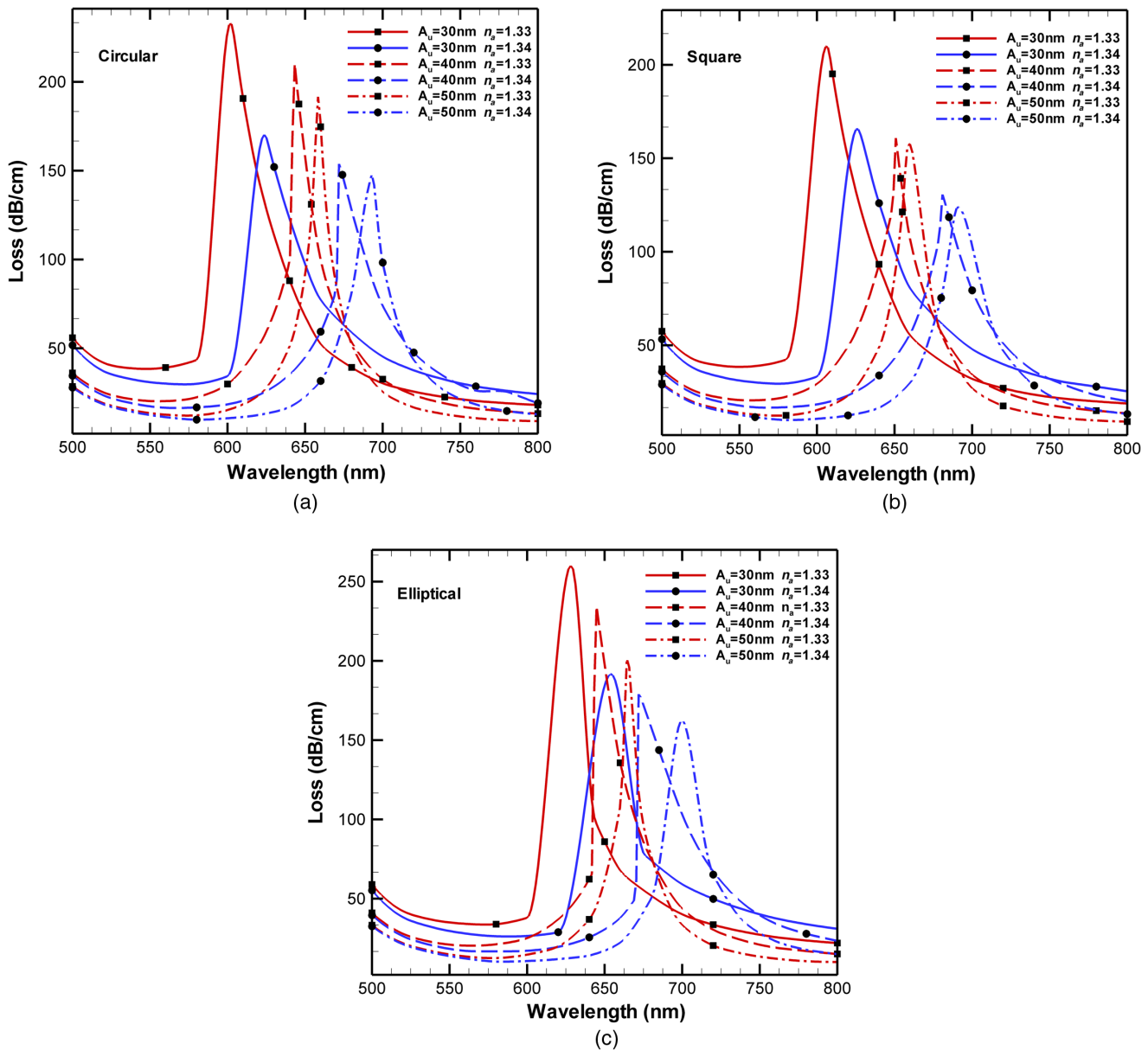|		*x*-polarized HE$_{11}^{x}$		*y*-polarized HE$_{11}^{y}$	
		Sensitivity	Resolution	Sensitivity	Resolution
n_a	Type	(nm/RIU)	(×10^{-5} RIU)	(nm/RIU)	(×10^{-5} RIU)
1.33 to 1.34	Circular	2900	3.5	4200	2.4
	Square	3100	3.2	3700	2.7
	Elliptical	2800	3.6	3300	3
1.34 to 1.35	Circular	3700	2.7	4000	2.5
	Square	3800	2.6	3900	2.6
	Elliptical	3600	2.7	3700	2.7

Fig. 5 The effect of gold layer thickness (t_{AU}) to loss with different wavelengths. The wavelengths are given for: (a) circular, (b) square, and (c) elliptical. [$n_a = 1.33$, $d_{1area} = 0.10$ $(\mu m)^2$, $d_{2area} = 0.25$ $(\mu m)^2$, and $d_{3area} = 0.14$ $(\mu m)^2$].

the metallic layer, the intensity of excitation is affected from the thickness of gold layer, where this is directly linked to the sensitivity of plasmon mode.[17]

Figures 5(a)–5(c) show the loss as a function of operating wavelength for various gold layer thicknesses. As can be seen from the figure, when the thickness of gold layer changed from 30 to 50 nm, the loss levels are decreasing while resonance peaks are shifted to longer wavelengths for all three types of geometries. This shows that, while gold layer thickness increases the light penetration inside the layers decreases, which results in lower loss levels. Moreover, it can be realized that square-based model exhibits lowest losses, whereas the elliptical-based model reaches the highest loss levels (strongest resonance) for all performed wavelengths. In contrast, leakage reduces at longer

wavelengths, where maximum losses are achieved at 30-nm gold thicknesses.

Next, Figs. 6(a)–6(c) show the effect of the central air hole on phase matching point of plasmon and fundamental core modes for various refractive indices. It can be seen that when the area of the central air hole is increasing from 0.08 $(\mu m)^2$ to 0.12 $(\mu m)^2$, the peak points are also shifting along the operating wavelength while the loss energy is reducing. Our numerical results show that phase matching points are so close to each other for all geometries. However, central hole with 0.10 $(\mu m)^2$ area shows overall the most consistent and optimized results for all proposed geometries.

Next, Figs. 7(a)–7(c) show the effect of the cladding air holes on phase matching point of plasmon and fundamental core mode. It can be easily realized from the figures that the
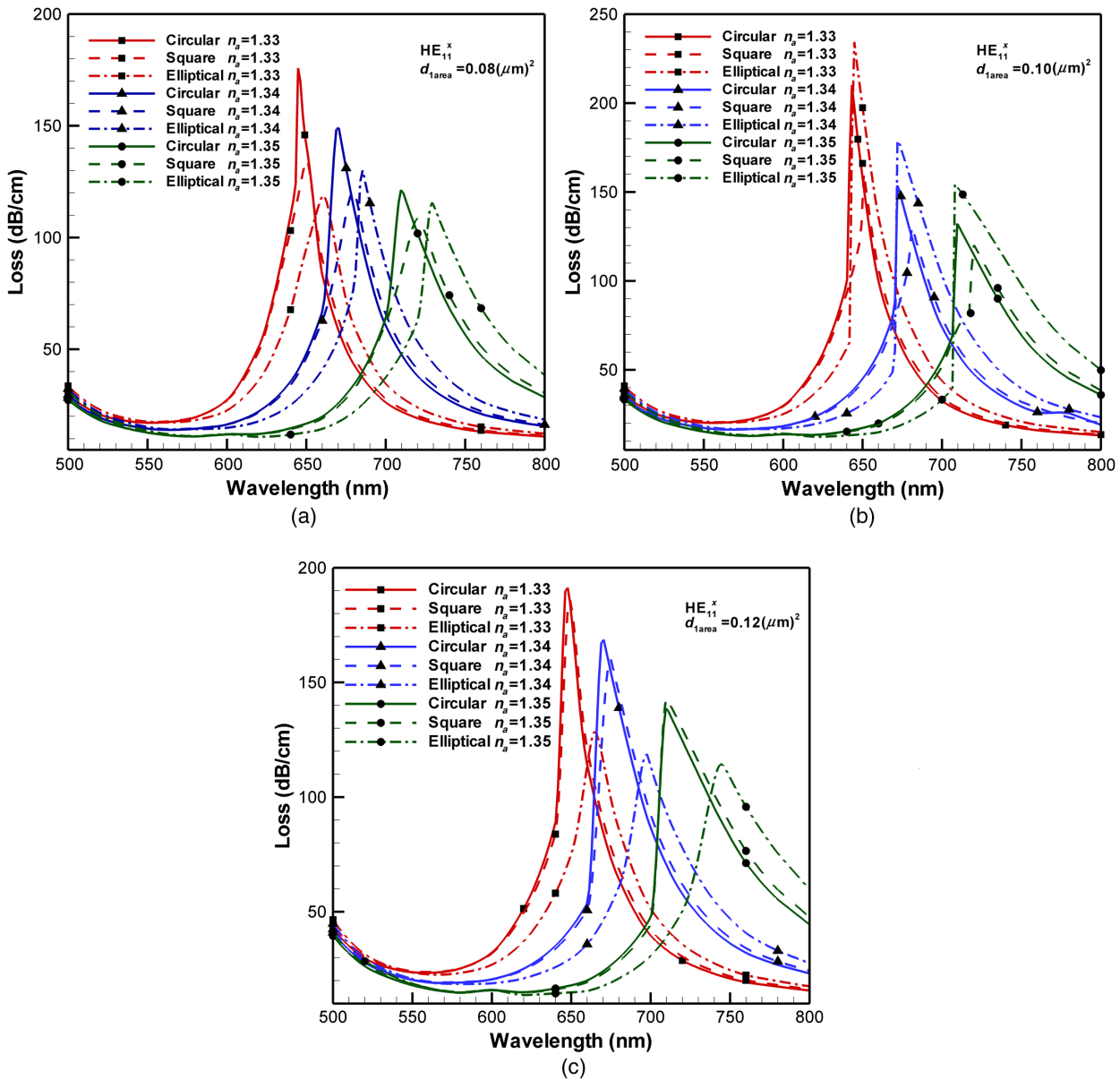
Fig. 6 The effect of central air hole (d_1) diameter to loss with regard to operating wavelengths. The areas for d_1 are given for: (a) 0.08 (μm)^2, (b) 0.10 (μm)^2, and (c) 0.12 (μm)^2. [$t_{AU} = 40$ nm, $d_{2area} = 0.25$ (μm)^2, and $d_{3area} = 0.14$ (μm)^2].

resonance peaks are shifted to shorter wavelengths and the loss levels are significantly increasing when air hole sizes are reduced 20% for all three types of geometries. However, it is worth noting that high propagation loss may limit the sensor's length to generate a measurable signal.[5,14]

The brief comparison of sensitivity and resolution of our proposed models is presented in Table 2. It is obvious that the design parameters and the plasmonic materials of listed studies are varying on each cited work. Therefore, fair comparisons of these results are not possible. However, it can be seen that numerical results reported in this study are comparable with previous studies. Among our numerical results, it seems that circular air hole-based model shows the best performance in terms of sensitivity, whereas the square- and elliptical-based models are also competitive since their sensitivities are fairly similar.

Another important factor that may affect the resonance condition is wavelength dependence of analyte refractive index. Figure 8 shows the wavelength dependency of water analyte, where water RI values are taken from Ref. 37. It can be seen that very negligible amount of change occurs on the resonance conditions for all geometries.

Finally, from a practical point of view it is critical to discuss the fabrication issues of the proposed sensor models. Due to the large analyte channels, production of the proposed models is possible. The high-pressure chemical vapor deposition technique[38] or then again, electroless plating techniques can be applied for depositing the gold layer.[39,40] Due to unrealistic fabrication targets, many theoretical models cannot be developed. The combined effects of surface tension and hole pressure during fiber drawing make it very difficult to control the shape of the holes in the fiber
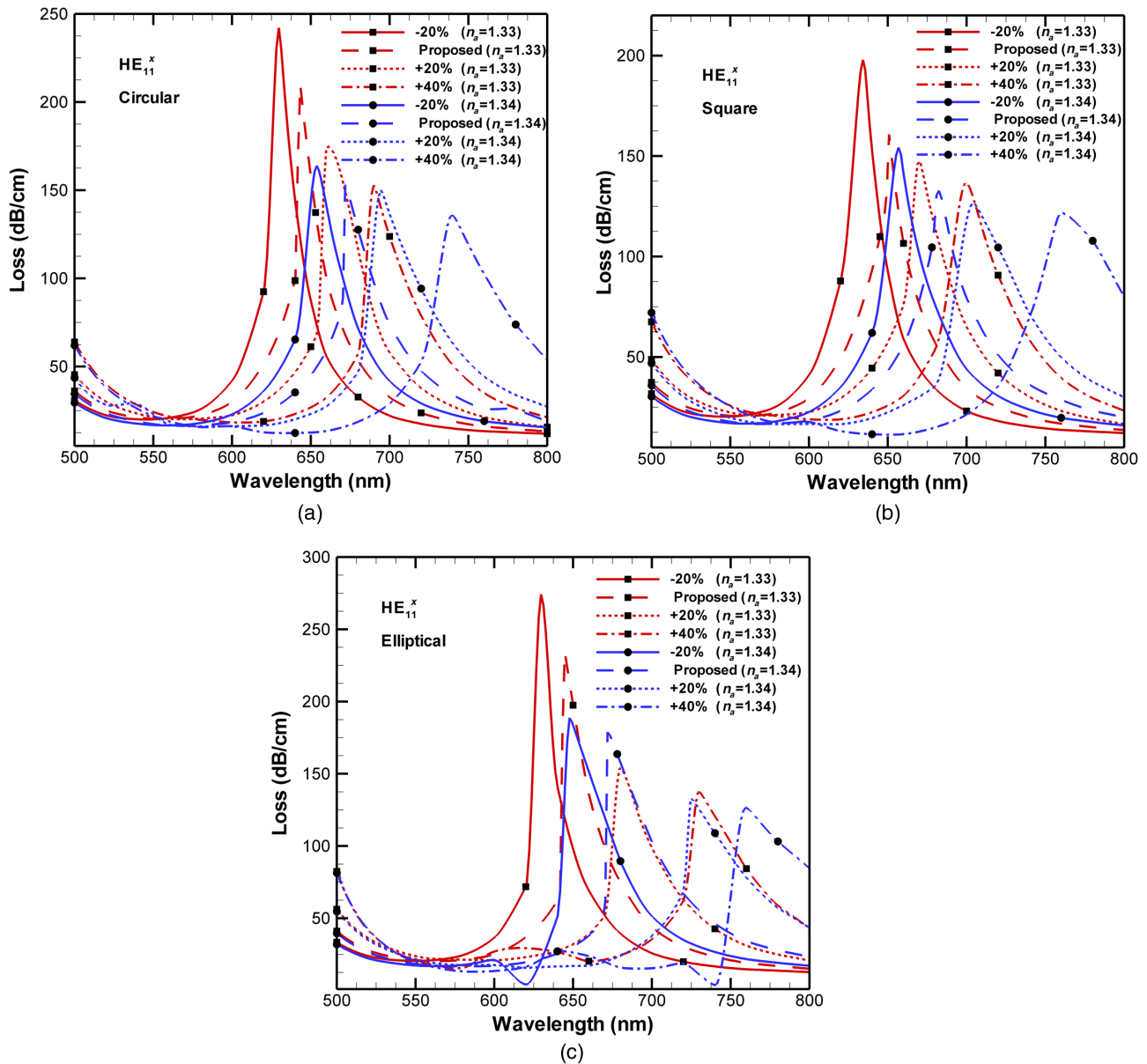
Fig. 7 The effect of air hole d_2 and d_3 diameters to loss for different wavelengths, (a) circular, (b) square, and (c) elliptical air hole-based PCF-SPR sensor designs. [$d_{1area} = 0.10 \ (\mu m)^2$, $t_{AU} = 40$ nm].

Table 2 Performance comparison of photonic crystal fiber-based SPR sensors.

| Characteristic design	Wavelength (nm)	Refractive index range	Sensitivity (nm/RIU)	Resolution (RIU)	Ref.
Ag-metalized SPR sensor	400 to 600	1.33 to 1.34	1167	8.57×10^{-5}	31
Large Ag-metalized SPR sensor	400 to 600	1.335 to 1.345	1500	6.67×10^{-5}	32
Birefringent SPR biosensor	500 to 800	1.33 to 1.34	2000	5×10^{-5}	21
Large Au-metalized SPR sensor	500 to 640	1.33 to 1.39	2000	5×10^{-6}	33
Exposed-core Grapefruit fibers based SPR sen.	460 to 620	1.33 to 1.34	2000	5×10^{-4}	34
Silver and graphene-doped SPR sensor	990 to 1200	1.46 to 1.49	3000	3.33×10^{-5}	14
Birefringence-based SPR sensor	540 to 660	1.33 to 1.34	3100	—	35
Gold–silver bimetallic fiber optic SPR sensor	500 to 800	1.33 to 1.34	3200	—	36
Two rings PCF SPR biosensor	500 to 750	1.33 to 1.37	4000	2.5×10^{-5}	30
Circular hole-based SPR sensor	500 to 800	1.33 to 1.35	4200	2.4×10^{-5}	This work
Square hole-based SPR sensor	500 to 800	1.33 to 1.35	3900	2.6×10^{-5}	This work
Elliptical hole-based SPR sensor	500 to 800	1.33 to 1.35	3700	2.7×10^{-5}	This work
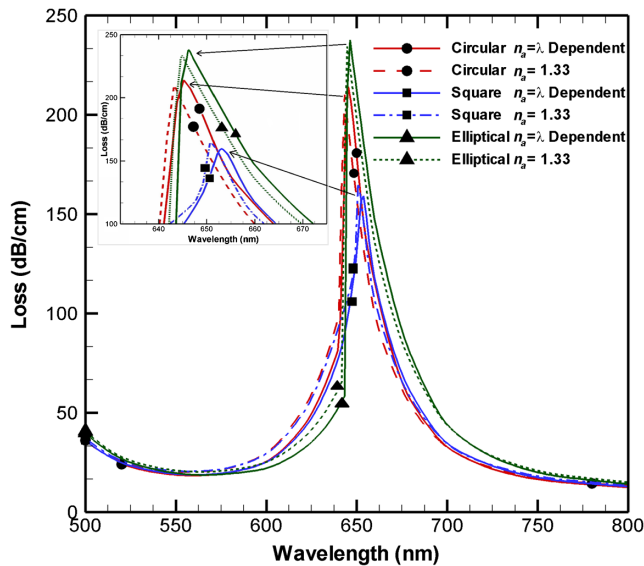
Fig. 8 The effect of wavelength dependences of analyte (water) refractive index to loss for HE_{11}^x [$t_{AU} = 40$ nm, $d_{1area} = 0.10$ $(\mu m)^2$, $d_{2area} = 0.25$ $(\mu m)^2$, and $d_{3area} = 0.14$ $(\mu m)^2$].

structure. This incident is one of the main problems in producing PCFs with noncircular holes. Apparently, developing rectangular air holes could be challenging with the traditional stack-and-draw method. Alternatively, the sol–gel method[41] provides additional design flexibility that will be necessary for such PCF structures, which allows for independent adjustment of the hole size, shape, and spacing. Also, newly developed slurry casting method[42] may be another alternative method for developing PCF structures with a highly flexible geometry.

4 Conclusion

In this study, we have numerically investigated PCF-based SPR sensor model with various air hole shapes. The phase matching conditions, loss analysis, and sensitivity of the proposed model have been investigated and compared thoroughly. The key design parameters such as gold layer thickness, cladding air holes, and the central air hole size of this specific model have also been studied. Numerical results have shown that SPR model based on circular air holes is more sensitive than elliptical- and square-based models. Sensitivity level of our proposed sensor design reaches to maximum 4200 and 3800 nm/RIU for y- and x-polarized core modes, respectively. These results are comparable with previously reported studies.

References

1. R. C. Jorgenson et al., "A fiber-optic chemical sensor based on surface plasmon resonance," *Sens. Actuators B Chem.* **12**(3), 213–220 (1993).
2. J. Homola et al., "Surface plasmon resonance sensors: review," *Sens. Actuators B Chem.* **54**(1), 3–15 (1999).
3. W. Qin et al., "Analyte-filled core self-calibration microstructured optical fiber based plasmonic sensor for detecting high refractive index aqueous analyte," *Opt. Lasers Eng.* **58**, 1–8 (2014).
4. J. C. Knight et al., "All-silica single-mode optical fiber with photonic crystal cladding," *Opt. Lett.* **21**(19), 1547–1549 (1996).
5. A. Hassani et al., "Design of the microstructured optical fiber-based surface plasmon resonance sensors with enhanced microfluidics," *Opt. Express* **14**(24), 11616–11621 (2006).
6. J. N. Dash et al., "SPR biosensor based on polymer PCF coated with conducting metal oxide," *IEEE Photonics Technol. Lett.* **26**(6), 595–598 (2014).
7. J. A. Kim et al., "Graphene based fiber optic surface plasmon resonance for bio-chemical sensor applications," *Sens. Actuators B Chem.* **187**, 426–433 (2013).
8. N. Luan et al., "Surface plasmon resonance temperature sensor based on photonic crystal fibers randomly filled with silver nanowires," *Sensors* **14**(9), 16035–16045 (2014).
9. A. Hassani et al., "Design criteria for microstructured-optical-fiber-based surface-plasmon-resonance sensors," *J. Opt. Soc. Am. B* **24**(6), 1423–1429 (2007).
10. B. D. Gupta, S. K. Srivastava, and R. Verma, *Fiber Optic Sensors Based on Plasmonics*, World Scientific, Singapore (2015).
11. A. A. Rifat et al., "Photonic crystal fiber based plasmonic sensors," *Sens. Actuators B Chem.* **243**, 311–325 (2017).
12. H. Ademgil et al., "PCF based sensor with high sensitivity, high birefringence and low confinement losses for liquid analyte sensing applications," *Sensors* **15**(12), 31833–31842 (2015).
13. C. J. Hao et al., "Surface plasmon resonance refractive index sensor based on active photonic crystal fiber," *IEEE Photonics J.* **5**(6), 4801108 (2013).
14. A. A. Rifat et al., "Photonic crystal fiber-based surface plasmon resonance sensor with selective analyte channels and graphene-silver deposited core," *Sensors* **15**(5), 11499–11510 (2015).
15. A. H. Bouk et al., "Dispersion properties of square-lattice photonic crystal fibers," *Opt. Express* **12**(5), 941–946 (2004).
16. H. Ademgil, "Highly sensitive octagonal photonic crystal fiber based sensor," *Optik* **125**(20), 6274–6278 (2014).
17. S. A. Razzak et al., "Chromatic dispersion properties of a decagonal photonic crystal fiber," in *Int. Conf. of Information and Communication Technology*, pp. 159–162, IEEE (2007).
18. G. Jiang et al., "High birefringence rectangular-hole photonic crystal fiber," *Opt. Fiber Technol.* **26**, 163–171 (2015).
19. S. Zhang et al., "Highly sensitive pressure-induced plasmon resonance birefringence in a silver-coated photonic crystal fiber," *J. Phys.* **276**(1), 012102 (2011).
20. M. Wang et al., "Simulation analysis of a temperature sensor based on photonic crystal fiber filled with different shapes of nanowires," *Optik* **126**(23), 3687–3691 (2015).
21. R. Otupiri et al., "A novel birefrigent photonic crystal fiber surface plasmon resonance biosensor," *IEEE Photonics J.* **6**(4), 1–11 (2014).
22. C. Liu et al., "Numerical analysis of a photonic crystal fiber based on a surface plasmon resonance sensor with an annular analyte channel," *Opt. Commun.* **382**, 162–166 (2017).
23. M. A. Al Mamun et al., "A square lattice photonic crystal fiber based surface plasmon resonance sensor with high sensitivity," in *Int. Conf. on Electrical Engineering and Information and Communication Technology*, pp. 1–5, IEEE (2014).
24. K. Saitoh et al., "Chromatic dispersion control in photonic crystal fibres: application to ultra-flattened dispersion," *Opt. Express* **11**(8), 843–852 (2003).
25. Y. Zhao et al., "Photonic crystal fiber based surface plasmon resonance chemical sensors," *Sens. Actuators B Chem.* **202**, 557–567 (2014).
26. C. Zhou, "Theoretical analysis of double-microfluidic-channels photonic crystal fiber sensor based on silver nanowires," *Opt. Commun.* **288**, 42–46 (2013).
27. M. Hautakorpi et al., "Surface-plasmon-resonance sensor based on three-hole microstructured optical fiber," *Opt. Express* **16**(12), 8427–8432 (2008).
28. Y. Y. Shevchenko et al., "Plasmon resonances in gold-coated tilted fiber Bragg gratings," *Opt. Lett.* **32**(3), 211–213 (2007).
29. E. K. Akowuah et al., "Numerical analysis of a photonic crystal fiber for biosensing applications," *IEEE J. Quantum Electron.* **48**(11), 1403–1410 (2012).
30. A. A. Rifat et al., "Surface plasmon resonance photonic crystal fiber biosensor: a practical sensing approach," *IEEE Photonics Technol. Lett.* **27**(15), 1628–1631 (2015).
31. L. Zheng et al., "Surface plasmon resonance sensors based on Ag-metalized nanolayer in microstructured optical fibers," *Opt. Laser Technol.* **43**(5), 960–964 (2011).
32. W. Wei et al., "Refractive index sensors based on Ag-metalized nanolayer in microstructured optical fibers," *Optik* **123**(13), 1167–1170 (2012).
33. P. Bing et al., "A surface-plasmon-resonance sensor based on photonic-crystal-fiber with large size microfluidic channels," *Opt. Appl.* **42**(3), 493–501 (2012).
34. X. Yang et al., "An exposed-core grapefruit fibers based surface plasmon resonance sensor," *Sensors* **15**(7), 17106–17114 (2015).
35. N. M. Y. Zhang et al., "Design and analysis of surface plasmon resonance sensor based on high-birefringent microstructured optical fiber," *J. Opt.* **18**(6), 065005 (2016).
36. E. K. Akowuah et al., "A highly sensitive photonic crystal fibre (PCF) surface plasmon resonance (SPR) sensor based on a bimetallic structure of gold and silver," in *4th Int. Conf. on Adaptive Science and Technology*, pp. 121–125, IEEE (2012).
37. S. Kedenburg et al., "Linear refractive index and absorption measurements of nonlinear optical liquids in the visible and near-infrared spectral region," *Opt. Mater. Express* **2**(11), 1588–1611 (2012).

38. P. J. Sazio et al., "Microstructured optical fibers as high-pressure micro-fluidic reactors," *Science* **311**(5767), 1583–1586 (2006).
39. J. A. Harrington, "A review of IR transmitting, hollow waveguides," *Fiber Integr. Opt.* **19**(3), 211–227 (2000).
40. N. Takeyasu et al., "Metal deposition deep into microstructure by electroless plating," *Jpn. J. Appl. Phys.* **44**(8L), 1134–1137 (2005).
41. R. T. Bise et al., "Sol–gel derived microstructured fiber: fabrication and characterization," in *Optical Fiber Communications Conf.*, OWL6, Vol. **3**, pp. 1–3 (2005).
42. T. Yajima et al., "Low-loss photonic crystal fiber fabricated by a slurry casting method," *Opt. Express* **21**(25), 30500–30506 (2013).

Ahmet Yasli received his BSc and MSc degrees from European University of Lefke and emerged as a gold medal student in both BSc and MSc studies in 2006 and 2008, respectively. Currently, he is working as a lab engineer at European University of Lefke and working toward his PhD in optical sensors. His field of interest and research is surface plasmon resonance-based photonic crystal fiber sensors.

Huseyin Ademgil received his BSc degree in electrical and electronic engineering from Eastern Mediterranean University in 2005. He received his MSc and PhD degrees from the University of Kent, Canterbury, UK, in 2006 and 2009, respectively. In September 2010, he joined European University of Lefke and was assigned as head of the Computer Engineering Department in 2013. His current research interests are mainly in the areas of optical sensing involving chemical and biomedical applications.